



Unstable Mixed Convection Flow in a Horizontal Porous Channel with Uniform Wall Heat Flux

A. Barletta¹ · D. A. S. Rees²

Received: 4 April 2019 / Accepted: 4 May 2019 / Published online: 14 May 2019
© Springer Nature B.V. 2019

Abstract

Buoyancy-induced instability of the horizontal flow in a plane-parallel porous channel is analysed. A model of momentum transfer is adopted where a quadratic form-drag contribution is taken into account. The basic fluid flow is parallel and stationary. Due to the uniform wall heating and the effect of the buoyancy, the velocity and the vertical temperature gradient depend on the vertical coordinate. The dynamics of small-amplitude perturbations on the basic mixed convection flow is studied numerically. Transverse, longitudinal and general oblique rolls are investigated. It is proved that the longitudinal rolls are the normal modes triggering the instability at the lowest Darcy–Rayleigh numbers. The condition of neutral stability is studied for different values of the form-drag parameter and of the Péclet number.

Keywords Porous medium · Form-drag effect · Uniform wall heating · Linear stability · Mixed convection

1 Introduction

There are several applications involving mixed convection flow in a porous channel. Such applications include the intensification of heat transfer in compact heat exchangers where metal foams are employed. In fact, for such porous media, the effective contact area between the fluid and the solid turns to be increased greatly, resulting in an enhancement of the heat transfer rate from the hot fluid.

Due to the very large porosity of metal foams, a departure from Darcy’s law behaviour is expected with a contribution of Forchheimer’s quadratic form-drag (Nield and Bejan 2017). This quadratic form-drag contribution may be merely a correction in the local momentum balance equation to be taken into account alongside the linear Darcy’s term, or even become dominant over such a linear term. It is well known that the form-drag term in the momentum balance for the seepage flow in porous media is modulated by the permeability-based

✉ A. Barletta
antonio.barletta@unibo.it

¹ Department of Industrial Engineering, Alma Mater Studiorum Università di Bologna, Bologna, Italy

² Department of Mechanical Engineering, University of Bath, Bath, UK

Reynolds number (Nield and Bejan 2017). The quadratic form-drag term becomes important when this Reynolds number is of order 1 or larger.

The form-drag effect influences not only forced convection flows, typical of the heat exchanger design, but also mixed convection flows. The thermal buoyancy may affect the parallel stationary flow in the channel or produce a secondary cellular flow. The second instance is typical of a developing convective instability. Conditions generating a convective instability often involve heating from below. A typical example is a plane porous channel where the lower boundary wall is kept at a uniform temperature larger than that imposed at the upper boundary wall. This set-up, characterised by a uniform throughflow, produces a convective instability studied by Prats (1966) by adopting Darcy's formulation of momentum transfer. The conclusions drawn from this author are that the critical Darcy–Rayleigh number, R , for the onset of instability is $4\pi^2$ and does not depend on the Péclet number relative to the basic flow rate.

A further development of this classical stability analysis was achieved by Rees (1997) on including the effect of the quadratic form-drag contribution in the local momentum balance. Rees (1997), in fact, proved that the Péclet number, P , influences the critical value of R for the transition to convective instability. The larger the intensity of the quadratic Forchheimer's term, the stronger is this influence. The overall effect of the form-drag contribution is a stabilisation of the horizontal throughflow. More results regarding possible variants of the Prats problem were obtained by Dodgson and Rees (2013) and by Rees and Mojtabi (2013). The former study deals with the effect of a time derivative term in the momentum balance, while the latter examines the thermal coupling with the conduction in bounding walls of non-negligible thickness. Further results regarding the stability analysis of the Prats problem (Prats 1966) with form-drag effect are relative to the onset of absolute instability (Delache et al. 2007), namely the unstable behaviour of localised wave packet perturbations acting on the base flow.

A different branch of studies has been focused on the case where the fluid-saturated porous channel undergoes a streamwise heating, so that the temperature gradient has both a vertical and a horizontal component (Nield et al. 1993; Manole et al. 1994; Barletta 2012). In practical cases, one can achieve such a condition when a uniform heat flux is prescribed at the bounding walls. Barletta (2012) examined the case where both walls are heated symmetrically. In this paper, it is shown that critical value of R for the onset of the instability depends on P and that no instability to small-amplitude perturbations is possible when $P < 19.1971$. Barletta et al. (2013) reconsidered the study carried out in Barletta (2012) by relaxing the hypothesis of inter-phase thermal equilibrium at the pore level. Sphaier and Barletta (2014) investigated the case where the lower wall is uniformly heated, while the upper wall is thermally insulated.

The objective of this paper is to develop further the analysis presented by Barletta (2012) on including the form-drag contribution in the model of momentum transfer. The form-drag term has different effects. It modifies the basic solution, and it yields a change in the formulation of the eigenvalue problem for the analysis of instability to small-amplitude perturbations. The latter analysis will be performed by means of a numerical solver. In particular, the shooting method implemented through an explicit Runge–Kutta technique will be adopted.

2 Governing Equations

We examine a horizontal plane porous channel having a thickness ℓ . The channel walls are impermeable and rigid. Both walls are heated with a uniform flux, $q_0 > 0$. A sketch of the channel is shown in Fig. 1.

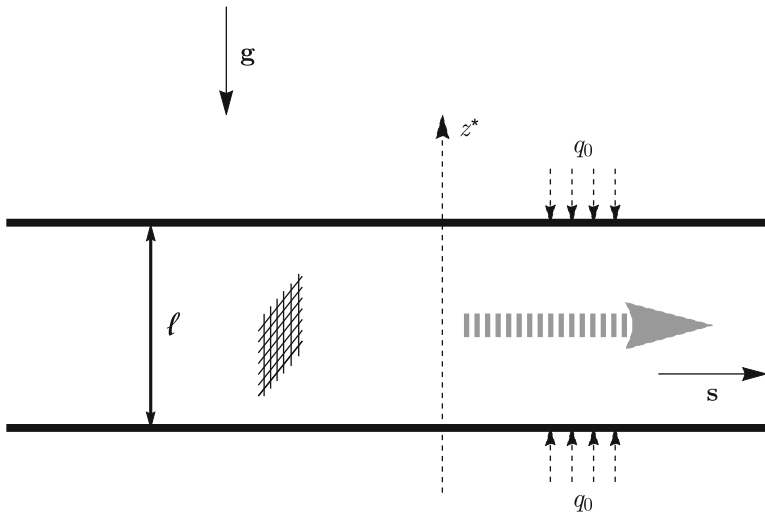


Fig. 1 Porous channel with horizontal throughflow

The Cartesian reference frame (x^*, y^*, z^*) is chosen so that the z^* -axis is vertical, while the (x^*, y^*) -axes are horizontal. Here, the starred symbols serve to denote the dimensional coordinates. The acceleration due to gravity is $\mathbf{g} = -g \mathbf{e}_z$, where g is its modulus, while \mathbf{e}_z is the z -axis unit vector. The buoyancy-induced flow is modelled by employing the Oberbeck–Boussinesq approximation and the Darcy–Forchheimer law. It is assumed that the porous medium is homogeneous and isotropic. The local energy balance is formulated by adopting a local thermal equilibrium scheme with a negligible effect of viscous dissipation. We mention that the form-drag effect is important when the fluid flow rate is high. However, a parametric domain may exist where the effect of thermal buoyancy is significant and the form-drag contribution is non-negligible. In particular, heat and momentum transfer in a porous medium with a high permeability reasonably displays this behaviour. This happens, for instance, when modelling fluid-saturated metal foams.

The local mass, momentum and energy balance equations are expressed in a dimensionless form as

$$\nabla \cdot \mathbf{u} = 0, \tag{1a}$$

$$\nabla \times [(1 + \xi|\mathbf{u}|)\mathbf{u}] = \nabla \times (T\mathbf{e}_z), \tag{1b}$$

$$\frac{\partial T}{\partial t} + \mathbf{u} \cdot \nabla T = \nabla^2 T, \tag{1c}$$

where the boundary conditions are written as

$$\begin{aligned} z = 0: \quad w = 0, \quad \frac{\partial T}{\partial z} = -R, \\ z = 1: \quad w = 0, \quad \frac{\partial T}{\partial z} = R. \end{aligned} \tag{2}$$

The dimensionless quantities employed in Eqs. (1) and (2) are the dimensionless position, $\mathbf{x} = (x, y, z)$, time, t , velocity field, $\mathbf{u} = (u, v, w)$ and temperature field, T . We also mention that Eq. (1b) represents the curl of the Darcy–Forchheimer local momentum balance equation, so that the dependence on the pressure gradient is encompassed.

The dimensional variables are denoted through starred symbols. Thus, the dimensionless quantities are obtained by the scaling,

$$\begin{aligned} (x^*, y^*, z^*) \frac{1}{\ell} &= (x, y, z), & t^* \frac{\alpha}{\sigma \ell^2} &= t, \\ (u^*, v^*, w^*) \frac{\ell}{\alpha} &= (u, v, w), & (T^* - T_0) \frac{g\beta K \ell}{\nu \alpha} &= T, \end{aligned} \tag{3}$$

where T_0 is a reference fluid temperature. The symbols K, α, β and ν denote the permeability, the average thermal diffusivity, the fluid thermal expansion coefficient and the kinematic viscosity, respectively. Moreover, σ is the heat capacity ratio, *i.e.* the ratio between the average volumetric heat capacity of the fluid-saturated porous medium and the volumetric heat capacity of the fluid.

The governing dimensionless parameters R and ξ are the Darcy–Rayleigh number and the form-drag parameter. They are given by

$$R = \frac{g\beta q_0 K \ell^2}{\nu \alpha \lambda}, \quad \xi = \frac{c_f \alpha \sqrt{K}}{\nu \ell}, \tag{4}$$

where λ and c_f are the average thermal conductivity and the form-drag coefficient, respectively. By considering a channel width $\ell \cong 1$ cm, since K is usually smaller than 10^{-4} cm² and c_f is smaller than 1 (Nield and Bejan 2017), the parameter ξ turns out to be 10^{-2} . If ℓ is smaller than 1 cm, then ξ would be larger, but the buoyancy force is likely to be negligible in this case, given that R scales with ℓ^2 .

3 The Stationary Buoyancy-Induced Flow

A steady mixed convection flow is implied by Eqs. (1) and (2) when the velocity field is assumed to be fully developed. This means that a basic solution is given by

$$\mathbf{u}_b = U(z) \mathbf{s}, \quad \nabla T_b = C \mathbf{s} + Q(z) \mathbf{e}_z, \tag{5}$$

where \mathbf{s} is an arbitrary unit vector lying in the (x, y) -plane (Fig. 1). One can determine the constant C and the functions $U(z)$ and $Q(z)$ by substituting Eq. (5) into Eqs. (1) and (2). We note that Eq. (2) is satisfied provided that $Q(0) = -R$ and $Q(1) = R$. On account of Eq. (1c), one obtains

$$Q(z) = -R + C \int_0^z U(\zeta) d\zeta, \tag{6}$$

where the dummy integration variable ζ is employed. A Péclet number, P , can be introduced so that

$$P = \int_0^1 U(\zeta) d\zeta. \tag{7}$$

Therefore, the boundary condition $Q(1) = R$ yields

$$C = 2R/P. \tag{8}$$

One may infer from Eq. (5) that C is the linear growth rate of T in the streamwise direction defined by the unit vector \mathbf{s} . Equation (8) allows one to conclude that this component of the

temperature gradient tends to infinity in the limiting case $P \rightarrow 0$. This feature is physically reasonable as the limit $P \rightarrow 0$ corresponds to the absence of flow along the channel. Under such conditions, a stationary state becomes incompatible with Eq. (2) as, for a net heating (cooling) of the fluid, the temperature would increase (decrease) unboundedly in time. It is not restrictive to assume $P > 0$, meaning a fluid flowing in the direction of s .

3.1 Unidirectional Flow

Equation (1b) can be rewritten as

$$[1 + \xi|U(z)|]U(z) = A - \frac{2R}{P}z, \tag{9}$$

where A is an integration constant. We will develop our analysis in a regime where $A > 0$ and $A > 2R/P$, so that the flow has a unique direction or, equivalently, $U(z) > 0$ for every z . We note that a fairly large P is needed for the form-drag effect to be important, namely having $P \sim O(1/\xi)$ or larger. Having estimated $\xi = 10^{-2}$, at its largest, this means having P of order 10^2 or larger. Thus, the assumption of unidirectional flow, $U(z) > 0$ for every z , appears to be realistic when the form-drag effect is non-negligible. On the other hand, a negligible form-drag effect changes Eqs. (6) and (9) into their Darcy’s law form, so that Eq. (5) yields just the same basic flow described in the paper by Barletta (2012). From Eq. (9), one obtains

$$U(z) = \frac{1}{2\xi} \left[\sqrt{4\xi \left(A - \frac{2R}{P}z \right) + 1} - 1 \right]. \tag{10}$$

Then, function $Q(z)$ is found by evaluating the integral in Eq. (6):

$$Q(z) = -R - \frac{Rz}{\xi P} + \frac{1}{12\xi^2} \left[(4A\xi + 1)^{3/2} - \left(4A\xi - \frac{8\xi Rz}{P} + 1 \right)^{3/2} \right]. \tag{11}$$

Finally, one can determine the constant A by employing the boundary condition $Q(1) = R$ or, equivalently, Eq. (7):

$$2R + \frac{R}{\xi P} - \frac{1}{12\xi^2} \left[(4A\xi + 1)^{3/2} - \left(4A\xi - \frac{8\xi R}{P} + 1 \right)^{3/2} \right] = 0. \tag{12}$$

The constant A can be obtained by finding the roots of this algebraic equation for fixed values of (ξ, R, P) . If one defines

$$\hat{A} = A - \frac{R}{P}, \tag{13}$$

we recognise that Eqs. (10)–(12) can be rewritten as

$$U(z) = \frac{1}{2\xi} \left\{ \sqrt{4\xi \left[\hat{A} - \frac{2R}{P} \left(z - \frac{1}{2} \right) \right] + 1} - 1 \right\}, \tag{14}$$

$$Q(z) = -R - \frac{Rz}{\xi P} + \frac{1}{12\xi^2} \left\{ \left[4 \left(\hat{A} + \frac{R}{P} \right) \xi + 1 \right]^{3/2} - \left[4 \left(\hat{A} + \frac{R}{P} \right) \xi - \frac{8\xi Rz}{P} + 1 \right]^{3/2} \right\}, \tag{15}$$

and

$$2R + \frac{R}{\xi P} - \frac{1}{12\xi^2} \left\{ \left[4 \left(\hat{A} + \frac{R}{P} \right) \xi + 1 \right]^{3/2} - \left[4 \left(\hat{A} - \frac{R}{P} \right) \xi + 1 \right]^{3/2} \right\} = 0. \tag{16}$$

It can be proved that the transformation,

$$R \rightarrow -R, \quad P \rightarrow P, \quad \xi \rightarrow \xi, \tag{17}$$

leaves Eq. (16) invariant. This means that under the transformation (17) the value of \hat{A} does not change. Moreover, the transformation (17) yields

$$U(z) \rightarrow U(1 - z), \quad Q(z) \rightarrow Q(1 - z). \tag{18}$$

This symmetry property of the basic solution yields important consequences regarding the behaviour when, instead of uniform wall heating, we have uniform wall cooling. In other words, we have a method to tackle the flow problem where, instead of $q_0 > 0$, we have $q_0 < 0$, and thus $R < 0$. The behaviour for wall cooling can immediately be inferred from that for wall heating by employing Eqs. (17) and (18). This means that reversing the sign of R is equivalent to a point reflection of the z -axis across $z = 1/2$, both for the basic velocity profile and for the basic temperature gradient along the vertical direction.

3.2 Darcy’s Law Limiting Case

In the limiting case where Darcy’s law holds, *i.e.* $\xi \rightarrow 0$, Eqs. (10)–(13) yield

$$A \cong P + \frac{R}{P}, \quad \hat{A} \cong P, \tag{19a}$$

$$U(z) \cong A - \frac{2R}{P} z = P - \frac{2R}{P} \left(z - \frac{1}{2} \right), \tag{19b}$$

$$Q(z) \cong -R + \frac{2AR}{P} z - \frac{2R^2}{P^2} z^2 = -R + 2R \left(1 + \frac{R}{P^2} \right) z - \frac{2R^2}{P^2} z^2. \tag{19c}$$

As anticipated, such expressions lead to the basic solution examined by Barletta (2012).

3.3 Large Péclet Number

Having specified that our interest is for a regime of fairly large Péclet numbers, it is interesting to explore what happens in a regime where $P \gg 1$. In fact, in such a regime Eqs. (10)–(12) undergo a drastic simplification, namely

$$A \cong \xi P^2 \cong \hat{A}, \tag{20a}$$

$$Q(z) \cong R(2z - 1), \tag{20b}$$

$$U(z) \cong P. \tag{20c}$$

Equations (20), together with Eq. (5), reveal that the regime attained for $P \gg 1$ is one of forced convection. In fact, there is a residual dependence on R in the expression of ∇T_b , suggesting an influence of the buoyancy. However, this dependence is just a consequence of the scale adopted in Eq. (3) to define the dimensionless temperature. A suitable redefinition of T , on dividing by R , makes ∇T_b independent of R . Another important consideration is that the limiting velocity profile, $U(z)$, and vertical temperature gradient, $Q(z)$, do not

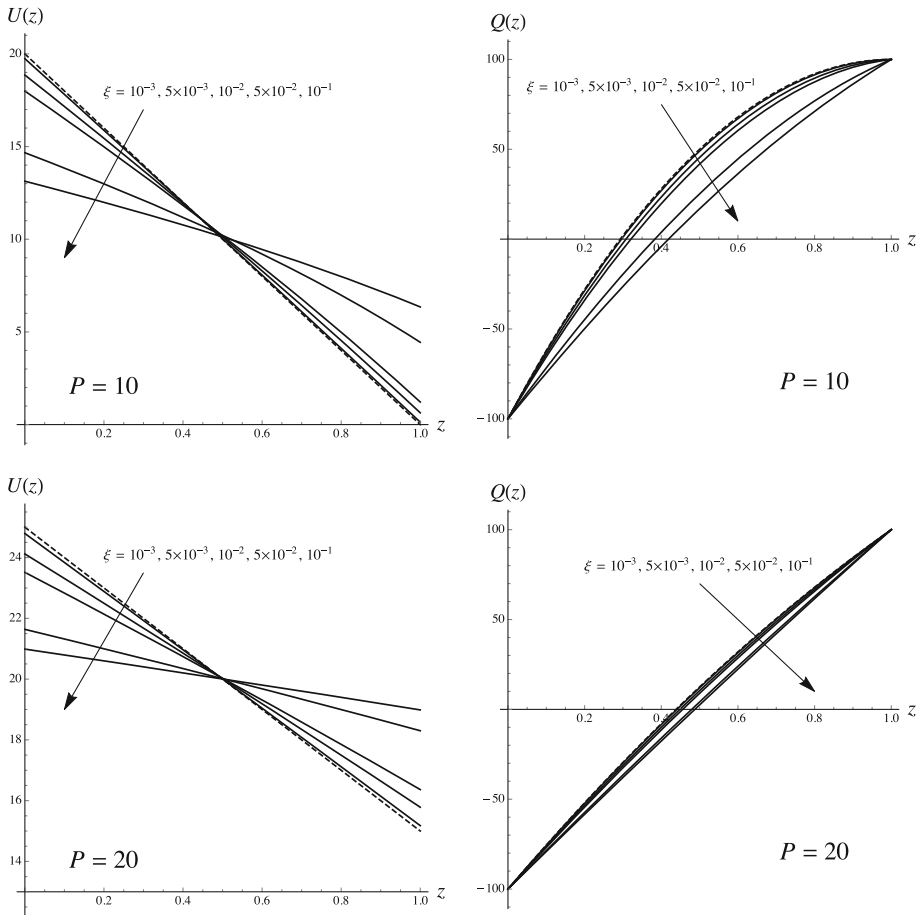


Fig. 2 Basic buoyant flow: velocity profile, $U(z)$, and vertical temperature gradient, $Q(z)$, when $R = 100$ and $P = 10$ or $P = 20$. The dashed lines denote the limiting case of Darcy’s law, $\xi \rightarrow 0$

depend on the form-drag parameter, ξ . This feature prefigures a situation where Darcy’s law determines the velocity profile and the temperature gradient of the basic flow in both limits $P \ll 1$ and $P \gg 1$. The domain where the departure from Darcy’s law is significant is, generally speaking, one of the intermediate values of P where $P \sim O(1/\xi)$ but not much larger. One must keep in mind that, in the regime $P \gg 1$, the form-drag contribution is still important with regards to the relationship between the flow rate and the pressure gradient. This aspect is unimportant for the forthcoming stability analysis of the basic solution, but it is an important feature testified by Eq. (9), where the constant \hat{A} , defined by Eq. (13), is in fact proportional to the imposed pressure gradient building up the flow rate. Equation (20a) shows that \hat{A} is proportional to the square of the flow rate, *i.e.* to P^2 , which is the expected behaviour when the form-drag contribution becomes dominant over Darcy’s contribution to the pressure gradient. In fact, we recall that Darcy’s law prescribes a contribution to the pressure gradient proportional to the flow rate.

The effect of the form-drag parameter, ξ , on the basic velocity profile, $U(z)$, and on the vertical temperature gradient, $Q(z)$, is illustrated in Fig. 2. Test cases are envisaged with

$R = 100$ and $P = 10$ or $P = 20$, where ξ ranges from 10^{-3} to 10^{-1} . On the basis of our considerations, values of ξ as large as 5×10^{-2} or 10^{-1} are hardly realistic. However, examining those cases is instructive as they illustrate situations, such as $P = 20$, where P is very large for saturated porous media and, simultaneously, $P \sim O(1/\xi)$. For $P = 20$, the influence of ξ on the velocity profile can still be important. On the other hand, the variability of $Q(z)$ with ξ is definitely small when $P = 20$. The limit of Darcy’s law, $\xi \rightarrow 0$, is also displayed with dashed lines, for comparison. The discrepancy between the solid lines corresponding to $\xi = 10^{-3}$ and the dashed lines is extremely small. As the buoyancy force induces departure from a uniform velocity profile, $U(z)$, Fig. 2 shows that this departure is smaller for larger values of ξ . In other words, the form-drag effect tends to assist the transition to a regime of forced convection as P increases. The larger the value of ξ , the smaller the Péclet number needed for such a transition. The last comment regarding Fig. 2 is that, strictly speaking, the velocity profile is linear only in the limit of Darcy’s law. However, the curvature is not very strong also with $\xi > 0$, so that in every case the profiles display a roughly linear trend. From the symmetry property described in Sect. 3.1, it is an easy task to obtain the plots of $U(z)$ and $Q(z)$ for $R = -100$ from those displayed in Fig. 2 for $R = 100$. Indeed, one has just to apply a point reflection of the z -axis across $z = 1/2$.

4 Stability Analysis

In order to carry out the stability analysis of the basic flow, expressed through Eqs. (5), (10) and (11), we write the velocity and temperature fields as

$$\mathbf{u} = \mathbf{u}_b + \tilde{\mathbf{u}}, \quad \nabla T = \nabla T_b + \nabla \tilde{T}, \tag{21}$$

where the perturbations are denoted as $\tilde{\mathbf{u}} = (\tilde{u}, \tilde{v}, \tilde{w})$ and \tilde{T} .

On assuming small-amplitude perturbations, we substitute Eq. (21) into Eqs. (1) and (2) and we neglect the terms of order higher than the first in the perturbations. As a result, we obtain the linearised governing equations and boundary conditions

$$\frac{\partial \tilde{u}}{\partial x} + \frac{\partial \tilde{v}}{\partial y} + \frac{\partial \tilde{w}}{\partial z} = 0, \tag{22a}$$

$$\begin{aligned} \xi U(z) \sin(2\phi) \frac{\partial \tilde{u}}{\partial z} + \xi \sin(2\phi) U'(z) \tilde{u} + \xi [3 - \cos(2\phi)] U'(z) \tilde{v} \\ + \{ \xi U(z) [3 - \cos(2\phi)] + 2 \} \frac{\partial \tilde{v}}{\partial z} - 2 [\xi U(z) + 1] \frac{\partial \tilde{w}}{\partial y} = -2 \frac{\partial \tilde{T}}{\partial y}, \end{aligned} \tag{22b}$$

$$\begin{aligned} \xi U(z) \sin(2\phi) \frac{\partial \tilde{v}}{\partial z} + \xi \sin(2\phi) U'(z) \tilde{v} + \xi [3 + \cos(2\phi)] U'(z) \tilde{u} \\ + \{ \xi U(z) [3 + \cos(2\phi)] + 2 \} \frac{\partial \tilde{u}}{\partial z} - 2 [\xi U(z) + 1] \frac{\partial \tilde{w}}{\partial x} = -2 \frac{\partial \tilde{T}}{\partial x}, \end{aligned} \tag{22c}$$

$$\begin{aligned} \xi U(z) \sin(2\phi) \left(\frac{\partial \tilde{u}}{\partial x} - \frac{\partial \tilde{v}}{\partial y} \right) - \{ \xi U(z) [3 + \cos(2\phi)] + 2 \} \frac{\partial \tilde{u}}{\partial y} \\ + \{ \xi U(z) [3 - \cos(2\phi)] + 2 \} \frac{\partial \tilde{v}}{\partial x} = 0, \end{aligned} \tag{22d}$$

$$\frac{\partial \tilde{T}}{\partial t} + \frac{2R}{P} (\tilde{u} \cos \phi + \tilde{v} \sin \phi) + Q(z) \tilde{w} + U(z) \left(\frac{\partial \tilde{T}}{\partial x} \cos \phi + \frac{\partial \tilde{T}}{\partial y} \sin \phi \right)$$

$$= \frac{\partial^2 \tilde{T}}{\partial x^2} + \frac{\partial^2 \tilde{T}}{\partial y^2} + \frac{\partial^2 \tilde{T}}{\partial z^2}, \tag{22e}$$

$$z = 0, 1: \quad \tilde{w} = 0, \quad \frac{\partial \tilde{T}}{\partial z} = 0, \tag{22f}$$

where Eq. (5) has been taken into account, primes denote derivatives with respect to z , and the unit vector \mathbf{s} along the direction of the basic flow is parameterised so that

$$\mathbf{s} = (\cos \phi, \sin \phi, 0), \tag{23}$$

with $0 \leq \phi \leq \pi/2$.

As the basic flow is inhomogeneous in the z -direction, we can analyse the dynamics of the perturbations by considering normal modes propagating along any direction in the (x, y) -plane. We have considered an arbitrary direction, \mathbf{s} , for the basic flow. This means that it is not restrictive to assume propagation of the normal modes along, say, the y -direction, provided that we let ϕ span all its possible values.

Notable cases are $\phi = 0$ meaning a basic flow along the x -axis and $\phi = \pi/2$ with the velocity being oriented in the direction of the y -axis. The former configuration is called longitudinal rolls, or L-rolls, while the latter case is called transverse rolls, or T-rolls. Intermediate cases with $0 < \phi < \pi/2$ are oblique rolls, or O-rolls.

A laboratory set-up producing the flow conditions given by Eq. (5) implies the existence of a lateral confinement with plane walls in the spanwise direction, perpendicular to \mathbf{s} . This implies that the plane channel has, in fact, a rectangular cross section with an arbitrary aspect ratio. The lateral boundaries may be assumed as adiabatic and impermeable. As a consequence, the O-rolls generally cannot satisfy these lateral boundary conditions, while L-rolls and T-rolls are allowed. With this reasoning in mind, in the following, we will mainly focus our stability analysis on L-rolls and T-rolls.

We can express the normal mode perturbations as

$$\tilde{\mathbf{u}} = \mathbf{q}(z) e^{iky} e^{\eta t}, \quad \tilde{T} = h(z) e^{iky} e^{\eta t}, \tag{24}$$

where k is the wave number, while the complex parameter η is such that its real part is the perturbation growth rate in time, while its imaginary part is $-\omega$, with ω denoting the angular frequency. The perturbation growth rate is the crucial parameter for instability: when positive the basic flow is unstable, when zero it is neutral stability, and when negative we have linear stability. The angular frequency marks the travelling or non-travelling nature of the normal mode, with ω/k meaning the phase velocity of the wave. Equation (24) implies that the normal mode perturbations do not depend on x .

In order to satisfy identically Eq. (22a), we define a streamfunction $\tilde{\psi}$ as

$$\tilde{v} = \frac{\partial \tilde{\psi}}{\partial z}, \quad \tilde{w} = -\frac{\partial \tilde{\psi}}{\partial y}. \tag{25}$$

Equations (24) and (25) require the existence of a function $f(z)$ such that

$$\tilde{\psi} = f(z) e^{iky} e^{\eta t}. \tag{26}$$

By substituting Eqs. (24)–(26) into Eqs. (22), we obtain an eigenvalue problem formulated through ordinary differential equations, namely

$$2[\xi U(z) + 1][2\xi U(z) + 1][\xi \tau U(z) + 2] f'' + 2\xi U'(z)\{2\xi U(z) [\xi \tau U(z) + 4] - \tau + 6\} f' - k^2[\xi U(z) + 1][\xi \tau U(z) + 2]^2 f - k[\xi \tau U(z) + 2]^2 h = 0, \tag{27a}$$

$$h'' - [k^2 + \eta + ik U(z) \sin \phi] h + \frac{4i R \sin \phi}{P} \frac{\xi U(z) + 1}{\xi \tau U(z) + 2} f' + k Q(z) f = 0, \tag{27b}$$

$$z = 0, 1: \quad f = 0, \quad h' = 0, \tag{27c}$$

where $\tau = 3 + \cos(2\phi)$. With L-rolls, we set $\phi = 0$ and Eqs. (27) are simplified as

$$[\xi U(z) + 1] (f'' - k^2 f) + \xi U'(z) f' - k h = 0, \tag{28a}$$

$$h'' - (k^2 + \eta) h + k Q(z) f = 0, \tag{28b}$$

$$z = 0, 1: \quad f = 0, \quad h' = 0. \tag{28c}$$

If we consider T-rolls, then $\phi = \pi/2$ so that Eqs. (27) yield

$$[2\xi U(z) + 1] f'' + 2\xi U'(z) f' - k^2 [\xi U(z) + 1] f - k h = 0, \tag{29a}$$

$$h'' - [k^2 + \eta + ik U(z)] h + \frac{2i R}{P} f' + k Q(z) f = 0, \tag{29b}$$

$$z = 0, 1: \quad f = 0, \quad h' = 0. \tag{29c}$$

4.1 The Limiting Case of Darcy’s Flow

In Sect. 3.2, we pointed out that the limit $\xi \rightarrow 0$ depicts the situation where the form-drag effect can be neglected and Darcy’s law holds. The asymptotic form of the basic solution in this limit is given by Eqs. (5) and (19). Thus, Eqs. (28) for L-rolls are written as

$$f'' - k^2 f - k h = 0, \tag{30a}$$

$$h'' - (k^2 + \eta) h - k \left[R - 2R \left(1 + \frac{R}{P^2} \right) z + \frac{2R^2}{P^2} z^2 \right] f = 0, \tag{30b}$$

$$z = 0, 1: \quad f = 0, \quad h' = 0. \tag{30c}$$

On the other hand, for T-rolls, Eqs. (29) yield

$$f'' - k^2 f - k h = 0, \tag{31a}$$

$$h'' - \left[k^2 + \eta + ikP - \frac{2ikR}{P} \left(z - \frac{1}{2} \right) \right] h + \frac{2iR}{P} f' - k \left[R - 2R \left(1 + \frac{R}{P^2} \right) z + \frac{2R^2}{P^2} z^2 \right] f = 0, \tag{31b}$$

$$z = 0, 1: \quad f = 0, \quad h' = 0. \tag{31c}$$

Both Eqs. (30) and (31) are in perfect agreement with the eigenvalue problem studied by Barletta (2012).

4.2 Large Péclet Number

In the asymptotic regime where $P \gg 1$, $\xi \ll 1$ and $P \sim O(1/\xi)$, Eqs. (20) and (27) yield

$$[\xi P (1 + \sin^2 \phi) + 1] f'' - k^2 [\xi P + 1] f - k h = 0, \tag{32a}$$

$$h'' - (k^2 + \hat{\eta}) h + 2kR \left(z - \frac{1}{2} \right) f = 0, \tag{32b}$$

$$z = 0, 1: \quad f = 0, \quad h' = 0, \tag{32c}$$

where we have

$$\hat{\eta} = \eta + ik P \sin \phi. \tag{33}$$

Obviously, $\hat{\eta}$ coincides with η for L-rolls ($\phi = 0$), while these quantities are different for T-rolls ($\phi = \pi/2$). The implicit assumption that $\hat{\eta}$ is finite, while P is extremely large means that, for T-rolls, both ω and kP become very large in this asymptotic regime, while their difference remains finite. For L-rolls, it is convenient to define

$$\theta = \frac{h}{\xi P + 1}, \quad \hat{R} = \frac{R}{\xi P + 1} \tag{34}$$

so that Eqs. (32) yield

$$f'' - k^2 f - k \theta = 0, \tag{35a}$$

$$\theta'' - (k^2 + \eta) \theta + 2k \hat{R} \left(z - \frac{1}{2} \right) f = 0, \tag{35b}$$

$$z = 0, 1: \quad f = 0, \quad h' = 0. \tag{35c}$$

Equations (35) show that, for longitudinal rolls, the neutral stability condition can be expressed as a function $\hat{R} = \hat{R}(k)$ which is independent of both ξ and P , provided that $P \gg 1$. On account of Eq. (34), one has $\hat{R}(k) = R(k)$ for $\xi \rightarrow 0$. Thus, one may evaluate the neutral stability function $R(k) = \hat{R}(k)$ in the Darcy’s law limit and deduce that, for $\xi > 0$, one has

$$R(k) = (\xi P + 1) \hat{R}(k). \tag{36}$$

It must be mentioned that this drastic simplification holds only for L-rolls, but it cannot be extended to T-rolls.

A stabilising effect of the form-drag contribution is inferred from Eq. (36). A similar stabilising effect was pointed out in the analysis of the Prats problem carried out by employing the Darcy–Forchheimer law, as reported by Rees (1997).

4.3 Numerical Solution

A numerical solution of the stability eigenvalue problem (27) can be obtained in order to evaluate the neutral stability condition, where $\Re(\eta) = 0$. The symbols \Re and \Im denote here the real and the imaginary parts of a complex number.

The first step is formulating the eigenvalue problem (27) as an initial value problem by assigning a sufficient number of extra conditions at $z = 0$, namely

$$f(0) = 0, \quad f'(0) = \gamma, \quad h(0) = 1, \quad h'(0) = 0. \tag{37}$$

The complex parameter γ is in fact unknown, and $h(0) = 1$ has been set to fix the otherwise arbitrary magnitude of the eigenfunctions (f, h) appearing in Eqs. (27). The system of differential equations given by Eqs. (27), together with the conditions (37) at $z = 0$, defines an initial value problem that can be solved with an explicit fourth-order Runge–Kutta method. Then, the target conditions at $z = 1$ stated in Eqs. (27) are used to obtain the value of γ , together with the eigenvalues. While the complex parameter γ is just an internal variable, entirely dependent on our arbitrary normalisation condition, $h(0) = 1$, and thus are devoid of any physical meaning, the eigenvalues are the clue of the stability analysis. The separation

Table 1 Longitudinal modes with $k = 3$, $P = 25$ and $\xi = 10^{-2}$: comparison between the neutral stability values of $(R, A, \omega - kP \sin \phi)$ obtained by a fixed step-size Runge–Kutta solver having gradually decreasing step size, δz , with those evaluated through an adaptive step-size Runge–Kutta solver

δz	R	A	$\omega - kP \sin \phi$
0.080	225.44737684	40.38863247	9.02739041
0.040	225.30912913	40.38295421	9.02184392
0.020	225.29990675	40.38257542	9.02146696
0.010	225.29931948	40.38255130	9.02144281
0.001	225.29928010	40.38254968	9.02144118
Adaptive	225.29928369	40.38254983	9.02144133

within Eqs. (27) between input parameters, known a-priori, and eigenvalues relies somewhat on an arbitrary selection. Our solution strategy is based on a scheme where

$$\begin{cases} \text{Input parameters} \implies \{\phi, P, \xi, k\}, \\ \text{Eigenvalues} \implies \{R, \omega\}. \end{cases} \tag{38}$$

As we are interested in the determination of the neutral stability condition, we recall that only the real part of η is fixed, and set to zero, while its imaginary part is to be determined. We also recall that the parameter A employed in the basic solution depends in an implicit manner on R, P and ξ through Eq. (12). Thus, finding the roots of Eq. (12) is part of the game when setting up the shooting method. Strictly speaking, the fulfilment of the target conditions,

$$f(1) = 0, \quad h'(1) = 0, \tag{39}$$

and of Eq. (12) is accomplished by adopting the Newton–Raphson method.

We mention that detailed presentations of the shooting method as applied to the solution of boundary value problems in fluid dynamics can be found in several textbooks. Among the many, we cite Chapter 19 of Straughan (2013) and Chapter 10 of Barletta (2019).

This numerical procedure has been tested by checking the results obtained by a fixed step-size Runge–Kutta scheme as compared with those produced by an adaptive step-size Runge–Kutta scheme. The test case is one involving O-rolls with $k = 3$ and $\phi = \pi/4$. We recall that ϕ denotes the inclination between the base flow direction and the x -direction, namely the direction parallel to the roll axis. The test case is one where $\xi = 10^{-2}$ and $P = 25$. In Table 1, a decreasing step size, δz , is considered with interval halving, and the output data R, A and $\omega - kP \sin \phi$ are compared with those obtained by employing the adaptive Runge–Kutta solver. It is clear from these data upon using the standard ratio test that these data have fourth-order accuracy, and if Richardson’s extrapolation formula is used, then these data show that the value of R , for example, is correct to 5 decimal places (8 significant figures), the correct value to 8 decimal places being 225.29928014. We also mention that $\omega - kP \sin \phi$ has been used instead of ω in order to subtract the contribution of the average flow rate in the direction of the normal mode from its angular frequency. We recall that, in the case of the Prats problem, this reduced angular frequency is precisely zero (Prats 1966). The excellent agreement between the fixed step-size scheme and the adaptive scheme is quantified by evaluating the relative discrepancy between any quantity, Q , among R, A and $\omega - kP \sin \phi$ as

$$\frac{\Delta Q}{Q} = \left| \frac{Q(\delta z = 0.001) - Q(\text{adaptive})}{Q(\text{adaptive})} \right|. \tag{40}$$

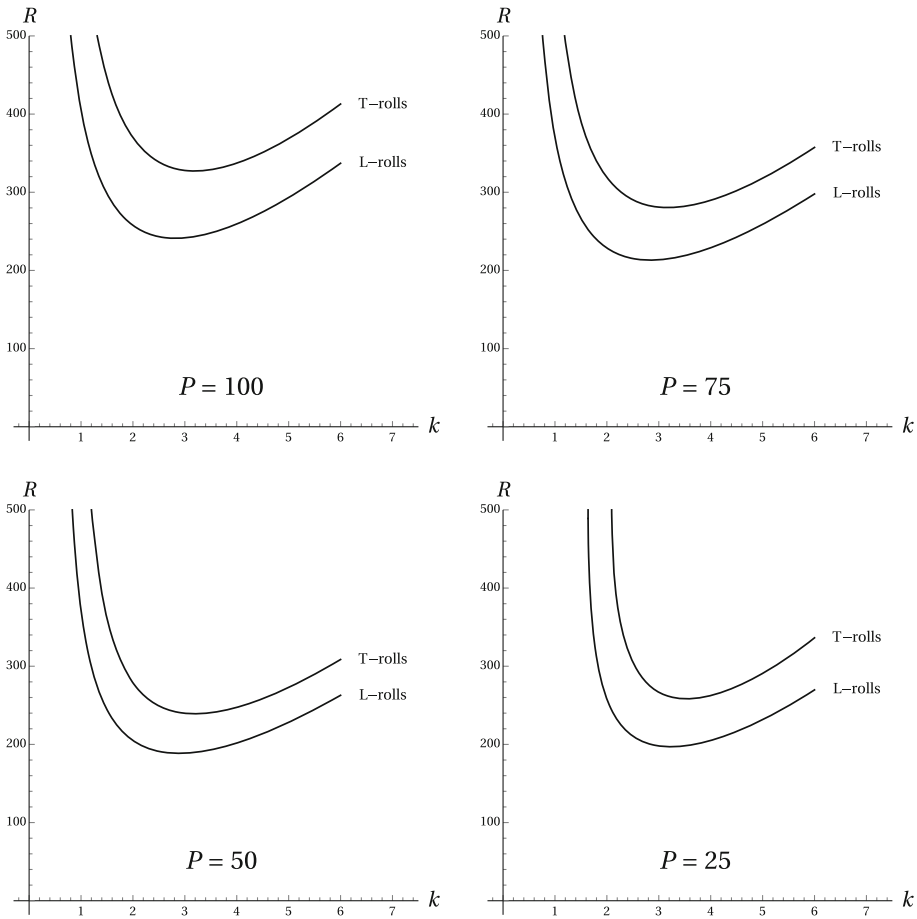


Fig. 3 Comparison between the neutral stability curves of L-rolls and T-rolls for $\xi = 10^{-2}$ and different values of P

The discrepancy is effectively evaluated by comparing the fixed step-size scheme with $\delta z = 10^{-3}$ with the adaptive scheme, as the effect of a decreasing step size is monotonic in the output data. The values of $\Delta R/R$ of $\Delta(\omega - kP \sin \phi)/(\omega - kP \sin \phi)$ are less than $2 \times 10^{-6} \%$, while that of $\Delta A/A$ is less than $4 \times 10^{-7} \%$. As a consequence of this test, we will generate all the numerical results presented in the forthcoming section by employing the adaptive step-size Runge–Kutta scheme.

5 Discussion of the Results

The transition to instability is described through the neutral stability curves in the (k, R) parametric plane. Such curves bound the instability region. Typically, instability is for values of R larger than those lying, for a given k , above the neutral stability curve. Hence, the point of minimum R at neutral stability is the endpoint for instability. This minimum, for prescribed (ξ, P) and for a given ϕ , yields the critical values (k_c, R_c, ω_c) . Plots of the neutral stability curves for $\xi = 10^{-2}$ are displayed in Fig. 3 for both L-rolls and T-rolls. Different

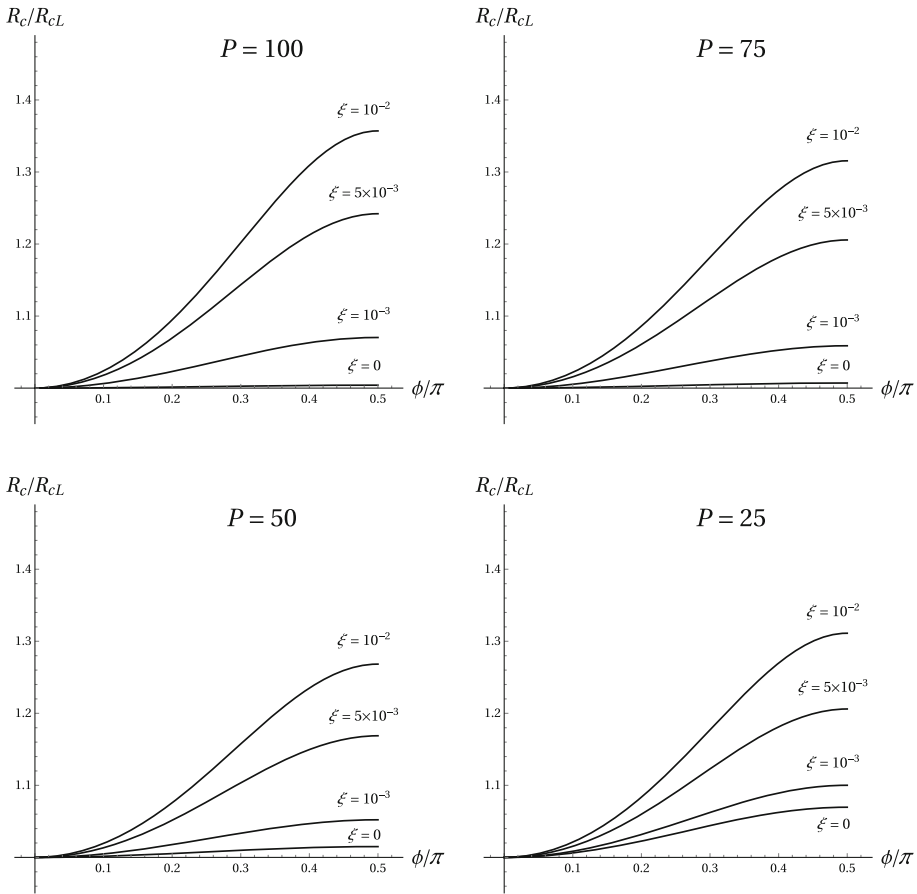


Fig. 4 Plots of the ratio R_c/R_{cL} versus ϕ/π , where R_{cL} is the value of R_c for L-rolls. Different frames are relative to different Péclet numbers, while different values of ξ are considered in each frame

Péclet numbers are considered with values decreasing from 100 to 25. In all frames, it is quite evident that the neutral stability curve for L-rolls lies below that for T-rolls, suggesting that the L-rolls are the most unstable modes. This feature is confirmed by Fig. 4 where the ratio between the critical Darcy–Rayleigh number R_c , evaluated for a given ϕ , and the critical value of R for L-rolls ($\phi = 0$) is plotted versus ϕ/π for different ξ and P . What comes out from Fig. 4 is quite evident: L-rolls are the normal modes yielding the smallest R_c with prescribed (ξ, P). One may also note that the larger the ξ , the wider the discrepancy between L-rolls and T-rolls. In other terms, the form-drag effect tends to strengthen the leading role of L-rolls in driving the system to instability. As a consequence, our forthcoming discussion will be confined to L-rolls.

An illustration of the neutral stability curves pertinent to L-rolls, where different values of ξ and P are examined, is shown in Fig. 5. The data for $\xi = 0$ are included to provide a comparison with the Darcy’s law case widely investigated in the paper by Barletta (2012). An evident aspect that can be inferred from Fig. 5 is that the form-drag effect is stabilising and that this feature is more and more marked as P increases. We mention that the same conclusion was reached while studying the behaviour of L-rolls in the large Péclet regime

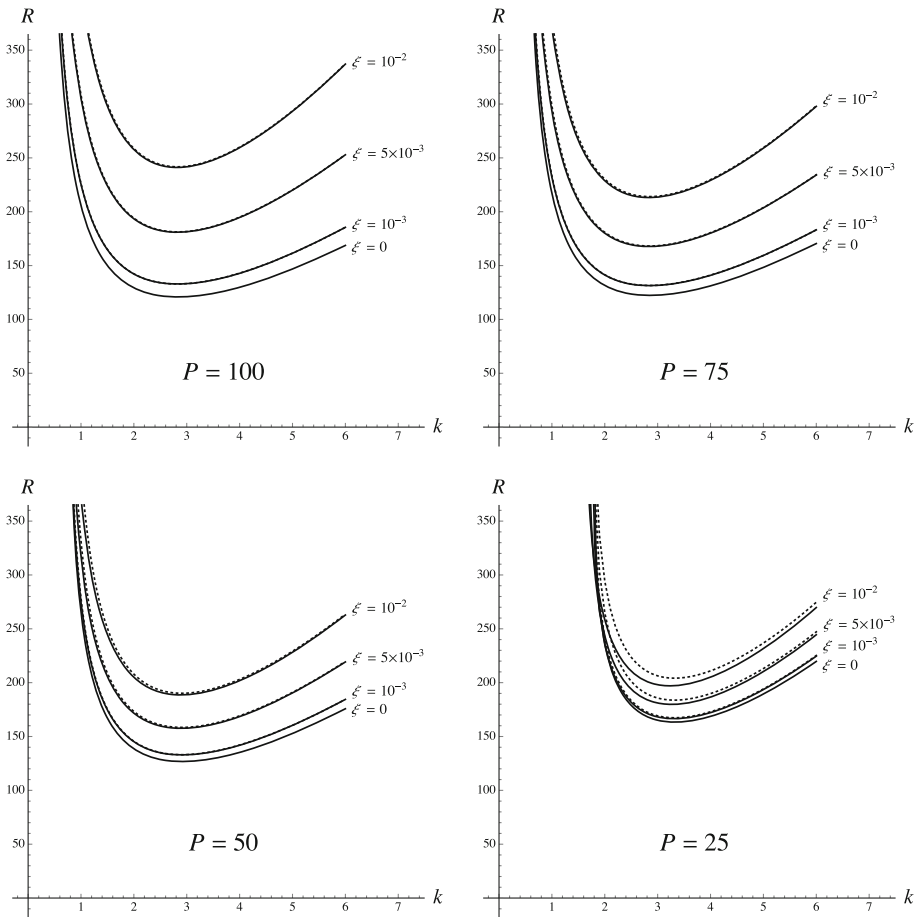
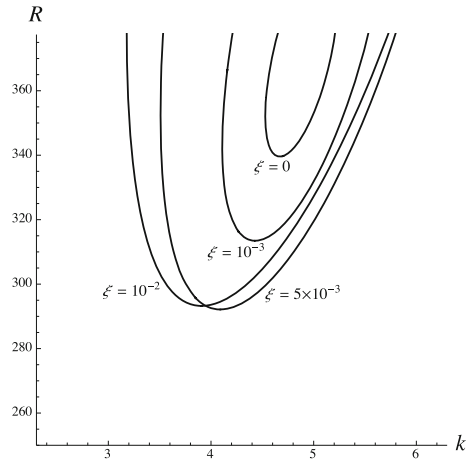


Fig. 5 L-rolls ($\phi = 0$): the solid lines are the neutral stability curves in the (k, R) -plane for prescribed (P, ξ) , while the dotted lines are relative to the asymptotic solution, Eq. (36), for $P \gg 1$

(Sect. 4.2). Figure 5 clearly shows that the discrepancy between the cases $\xi = 0$ and $\xi = 10^{-3}$ is not very large becoming smaller and smaller as P decreases. In fact, as P decreases, the form-drag effect on the neutral stability condition is gradually attenuated. Such a behaviour is reasonable given that the order of magnitude of the form-drag contribution to the flow rate is ξP . One may notice a slight exception to the general destabilising effect of the form-drag contribution displayed in the case $P = 25$ when small values of k are involved. This exception has a minor interest for our analysis as it does not alter the monotonic increasing trend of R_c with ξ . Even if barely visible with $P = 100, 75$ and 50 , Fig. 5 displays with dotted lines the neutral stability curves obtained by using the $\xi = 0$ solution and Eq. (36) or, in other terms, the approximation for large Péclet numbers. The dotted lines are very close to the corresponding solid lines with a more visible dissimilarity in the case $P = 25$. For a given P , the discrepancy between dotted lines and solid lines is larger if ξ is larger, thus corroborating that what makes the bulk influence is the value of ξP . Again, Eq. (36) motivates this finding.

Fig. 6 L-rolls ($\phi = 0$): neutral stability curves with $P = 19.22$ and prescribed values of ξ



The stabilising role of the form-drag effect is ultimately lost when we consider values of P which are significantly small, as illustrated by Fig. 6. On studying the Darcy's law regime, *i.e.* the case $\xi = 0$, Barletta (2012) proved that the neutral stability curves become closed loops when P is sufficiently small and, for $P = 19.1971$, they shrink to a point and then they disappear. This means that instability is out of reach when P is smaller than this threshold value. We also remark that a closed-loop shape of the neutral stability curve implies that instability is possible only within a compact and bounded region of the (k, R) -plane with stability happening all around this isolated region. The form-drag effect for values of P close to this threshold can be discerned in Fig. 6. In fact, this figure is relative to $P = 19.22$. An increasing ξ yields a non-monotonic change in the critical value of R , which decreases for smaller values of ξ , but then starts increasing when ξ changes from 5×10^{-3} to 10^{-2} . At this point of our discussion of the results, it is worth recalling that our study is grounded on the hypothesis of unidirectional basic velocity profile or, equivalently, $A > 2R/P$. The parametric range displayed in Fig. 6 is chosen so that this constraint is satisfied. On a larger range, the neutral stability curves for different ξ are in fact closed loops that, eventually, are likely to shrink and collapse to a point for values of P smaller than 19.22.

The features of the transition to instability in the regime of P slightly smaller than 20 become evident on plotting the critical values of R and k versus P . Figure 7 shows that, when P approaches 20 from above and slightly decreases below this value, both R_c and k_c undergo a steep increase. This behaviour is that marking the closed loops of neutral stability which gradually shrink, collapse to a point and then disappear, as mentioned above and quantitatively described by Barletta (2012) for the case $\xi = 0$. Figure 7 also shows the interchange between the stabilising and destabilising roles of the form-drag contribution in a regime of relatively small Péclet numbers. This feature is found when the plots of R_c versus P for different ξ intersect. Figure 7 also provides an exploitation of the regime described by Eq. (36). The large Péclet regime, in fact, features linear trends of R_c versus P , with k_c becoming independent of ξ . All these consequences of Eq. (36) are visible in Fig. 7. Another feature worth being highlighted is the non-monotonic trend of R_c versus P for a given, sufficiently large, ξ . A minimum is displayed showing up the different features of the large- P regime as compared with that arising close to the lowest possible P for the onset of instability. We finally note that the dotted lines represented in Fig. 7 reflect the asymptotic regime given by Eq. (36). They are overlapped by the solid lines except for cases with a large ξ and P close to 20.

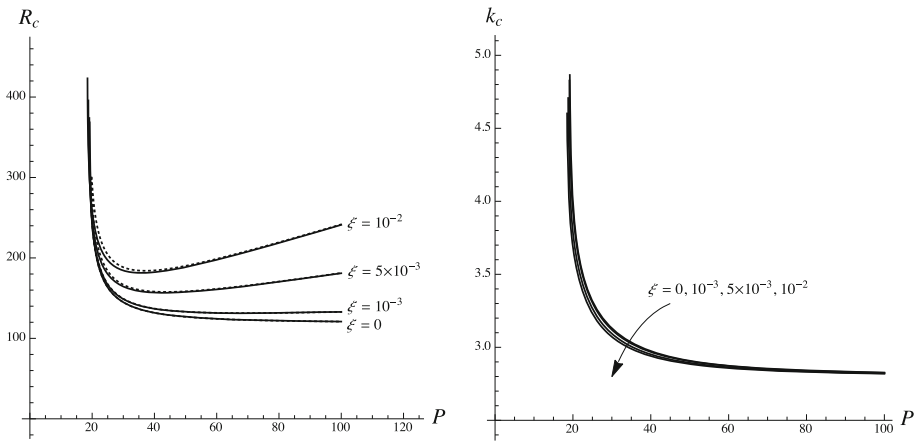


Fig. 7 L-rolls ($\phi = 0$): plots of R_c and k_c versus P , for prescribed values of ξ . The dotted lines are relative to the asymptotic regime with $P \gg 1$, considered in Eq. (36)

Given what we found in Sect. 3.1 regarding the case of wall cooling, i.e. $R < 0$, we can easily conclude that the neutral stability condition for that case is with $R = -R(k)$. Here, $R(k)$ is the neutral stability curve for the case of wall heating, whose properties have been discussed above. This conclusion can be inferred from Eqs. (27) by recognising that the stability eigenvalue problem is left invariant by simultaneously applying a point reflection of the z -axis across $z = 1/2$ and a sign change of R .

We finally comment on the assumption, formulated in Sect. 3.1, regarding the unidirectional nature of the basic flow. All the numerical examples of neutral stability presented in this paper have been reported by excluding those data where the assumed condition $A - 2R/P > 0$ is violated. Incidentally, we mention that the only severe exclusions were done for the lowest values of P compatible with the existence of an instability. This happens when we are slightly below $P = 20$. Here, the neutral stability curves are relative to very high values of R so that $A - 2R/P$ may well become zero or negative. Thus, in order to exclude cases where $A - 2R/P < 0$, in Fig. 6, the neutral stability curves have been cut at larger values of R . This is not a true limitation in the potentially informative content of this figure. In fact, one should not forget that the bulk knowledge gathered from a linear stability analysis is the critical condition (k_c, R_c) and, hence, the minima of the neutral stability curves.

6 Conclusions

Convective flow in a horizontal porous channel has been studied. The upper and lower impermeable boundaries are subject to symmetric uniform heat fluxes. Such a condition yields a uniform heating or cooling depending on the sign of the Darcy–Rayleigh number, R . The analysis has been carried out with the understanding that the channel is heated through its boundaries ($R > 0$). However, a symmetry in the mathematical formulation of the problem has been proved which allows a straightforward extension of the results to the uniform cooling case ($R < 0$). The flow in the porous medium has been modelled by including the form-drag effect and, hence, by adopting the Darcy–Forchheimer law. A steady-state basic solution has been found, which depends on the form-drag parameter, ξ , on the Péclet number, P , as well as on R . The main features of the basic solution have been pointed out by focusing

our attention on a situation where the flow is unidirectional across the channel cross section. On adopting a streamfunction–temperature formulation, we expressed the linear dynamics of small-amplitude perturbations through a system of ordinary differential equations. This then is the stability eigenvalue problem, whose numerical solution has led us to the neutral stability curves $R(k)$, where k is the wave number, for different pairs (P, ξ) . The principal results found from the linear stability analysis can be outlined as follows:

- Given that the analysis has been carried out for longitudinal, transverse and oblique rolls, the most unstable modes of perturbation turned out to be the longitudinal rolls.
- There exists a wide domain in the parametric plane (P, ξ) where the neutral stability condition can be straightforwardly gathered from that obtained in the Darcy's flow regime, *i.e.* in the asymptotic case $\xi \rightarrow 0$. There is, in fact, an approximate expression of $R(k)$ where the neutral stability function obtained for $\xi \rightarrow 0$ is merely scaled with the multiplying factor $\xi P + 1$. This regime is attained for large Péclet numbers, such that $\xi \ll 1$ and $P \sim O(1/\xi)$.
- The influence of P on the critical value of R for the onset of the instability is non-monotonic, as an increasing value of P tends to be markedly destabilising, for smaller P , and stabilising, for larger values of P . The latter behaviour is mainly triggered by the form-drag contribution.
- The onset of instability for conditions of wall heating ($R > 0$) and wall cooling ($R < 0$) is perfectly symmetric. In fact, in these two cases, the absolute value of $R(k)$ versus k for every given pair (P, ξ) is exactly the same. What changes is just the sign.

References

- Barletta, A.: Thermal instability in a horizontal porous channel with horizontal through flow and symmetric wall heat fluxes. *Transp. Porous Media* **92**, 419–437 (2012)
- Barletta, A.: *Routes to Absolute Instability in Porous Media*. Springer, New York (2019)
- Barletta, A., Celli, M., Kuznetsov, A.V.: Convective instability of the Darcy flow in a horizontal layer with symmetric wall heat fluxes and local thermal nonequilibrium. *ASME J Heat Transfer* **136**, 012601 (2013)
- Delache, A., Ouarzazi, M.N., Combarous, M.: Spatio-temporal stability analysis of mixed convection flows in porous media heated from below: comparison with experiments. *Int. J. Heat Mass Transfer* **50**, 1485–1499 (2007)
- Dodgson, E., Rees, D.A.S.: The onset of Prandtl–Darcy–Prats convection in a horizontal porous layer. *Transp. Porous Media* **99**, 175–189 (2013)
- Manole, D.M., Lage, J.L., Nield, D.A.: Convection induced by inclined thermal and solutal gradients, with horizontal mass flow, in a shallow horizontal layer of a porous medium. *Int. J. Heat Mass Transfer* **37**, 2047–2057 (1994)
- Nield, D.A., Bejan, A.: *Convection in Porous Media*, 5th edn. Springer, New York (2017)
- Nield, D.A., Manole, D.M., Lage, J.L.: Convection induced by inclined thermal and solutal gradients in a shallow horizontal layer of a porous medium. *J. Fluid Mech.* **257**, 559–574 (1993)
- Prats, M.: The effect of horizontal fluid flow on thermally induced convection currents in porous mediums. *J. Geophys. Res.* **71**, 4835–4838 (1966)
- Rees, D.A.S.: The effect of inertia on the onset of mixed convection in a porous layer heated from below. *Int. Commun. Heat Mass Transfer* **24**, 277–283 (1997)
- Rees, D.A.S., Mojtabi, A.: The effect of conducting boundaries on Lapwood–Prats convection. *Int. J. Heat Mass Transfer* **65**, 765–778 (2013)
- Sphaier, L.A., Barletta, A.: Unstable mixed convection in a heated horizontal porous channel. *Int. J. Therm. Sci.* **78**, 77–89 (2014)
- Straughan, B.: *The Energy Method, Stability, and Nonlinear Convection*. Springer, New York (2013)